

Symmetry breaking of large-amplitude parametric oscillations in a few-layer graphene nanomechanical resonator

Chen Yang,^{1,2} YuBin Zhang,^{1,2} Heng Lu,^{1,2} Ce Zhang,^{1,2} FengNan
Chen,^{1,2} Ying Yan,^{1,2} Fei Xue,³ Alexander Eichler,⁴ and Joel Moser^{1,2,*}

¹*School of Optoelectronic Science and Engineering & Collaborative
Innovation Center of Suzhou Nano Science and Technology,
Soochow University, 215006 Suzhou, China*

²*Key Lab of Advanced Optical Manufacturing Technologies of Jiangsu Province
& Key Lab of Modern Optical Technologies of Education Ministry of China,
Soochow University, 215006 Suzhou, China*

³*School of Physics, Hefei University of Technology, 230601 Hefei, China*

⁴*Laboratory for Solid State Physics,
ETH Zürich, 8093 Zürich, Switzerland*

(Dated: February 27, 2025)

Abstract

Graphene nanomechanical resonators are well suited for the study of parametric oscillations. Their large frequency tunability and their pronounced nonlinearities enable an efficient modulation of their resonant frequency. Here, we present measurements of the response of a few-layer graphene nanomechanical resonator driven by a large parametric pump at frequency 2ω and a weak external drive at ω , where ω is set near the mechanical resonant frequency ω_0 . The pump actuates the resonator beyond the threshold for large-amplitude parametric oscillations, while the drive breaks the symmetry of the parametric phase states. By increasing and decreasing a gate voltage to detune ω_0 in the presence of the pump and the drive, we observe a double hysteresis in the response. The double hysteresis reveals the existence of two possible large-amplitude vibrational states whose phase difference is nearly π radians. We deterministically prepare the resonator in either one of these states by cycling the gate voltage. We measure the stationary occupation probabilities of the two states in the presence of a white Gaussian force noise, and find that they strongly depend on the amplitude and on the phase of the external drive. Parametric oscillations with broken phase symmetry hold promise as units of binary information. Their phase states can be mapped to biased bi-modal degrees of freedom, such as Ising spins in an external magnetic field. Our work invites future studies on coupled graphene parametric resonators whose phase states may be mapped to a system of Ising spins.

A mechanical parametric resonance is the state of a resonator driven by the modulation of its spring constant beyond a threshold [1–6]. The dynamics of a parametric resonator results from an interplay between the parametric excitation (the pump), the linear and the nonlinear restoring forces, and mechanical dissipation [7, 8]. It is governed by the depth λ and the angular frequency ω_p of the modulation of the spring constant k_0 as a function of time t , $k_0 \rightarrow k_0(1 - \lambda \cos \omega_p t)$. Where λ is large enough that the rate of energy supplied by the pump compensates for dissipation, and with ω_p close to twice the vibrational resonant frequency ω_0 , the effective damping of the resonator becomes negative and the resonator enters a regime of large-amplitude oscillations near ω_0 [7]. In the absence of an external drive near ω_0 , the parametric resonator hosts one of two possible vibrational states whose amplitudes are equal and whose phases differ by π radians. Both states are equally likely

* j.moser@suda.edu.cn

to be actuated by the pump –experimentally, this can be seen by injecting a force noise to toggle the resonator between its two stable states stochastically, resulting in two equally distributed populations [9–15]. These ‘phase states’ are interesting, in part because they are the states of the parametron employed in early digital computing systems [16]. There, binary information was encoded in the phase of electrical parametric oscillations. Similarly, the phase of nanomechanical parametric vibrations can be mapped to the states of a classical bit, enabling nanomechanical logic operations [17] and the emulation of Ising spins [18–21]. A prerequisite for the direct control of the phase states is the breaking of their symmetry, which can be realized by adding a nearly-resonant external drive to the parametric excitation [9, 22, 23]. Far away from resonance, the resonator responds mostly to this external drive, which means that the vibrational phases far below and far above resonance differ by π radians. Adiabatically sweeping the angular frequency of the drive ω_d and that of the pump $\omega_p \simeq 2\omega_d$ through resonance ensures that the parametric resonator selects states with the phase imprinted by the external drive off resonance [9, 22, 24, 25]. A striking phenomenon that accompanies an upward and downward frequency sweep is the appearance of a double hysteresis in the amplitude and in the phase of the vibrational response [22, 26]. It arises from the nonlinear response to the compound excitation. It is within this double hysteresis that the two phase states can be individually addressed.

Low-dimensional nanomechanical resonators built on a chip, such as nanotubes, nanowires, nanobeams, nanoplates, and atomically-thin membranes [27, 28], possess two characteristics that are advantageous for parametric oscillators. Firstly, their resonant frequencies are highly tunable with a dc voltage applied to a nearby electrode [29, 30], which implies that ω_0 can be efficiently modulated by electrical means to excite parametric modes [2–5, 31, 32]. Secondly, they feature pronounced conservative [29, 33–36] and dissipative mechanical nonlinearities [7, 37–39], which favor the observation of the double hysteresis mentioned above [22, 26]. Among low-dimensional nanomechanical resonators, graphene resonators are generally interesting because their resonant frequencies are high, they dissipate little energy at low temperature, and they can be carved into large arrays [40]. High resonant frequencies enable double hystereses whose jumps are separated clearly in frequency, making them easily identifiable. Low dissipation enables large-amplitude parametric oscillations beyond a moderate pump power. Large arrays may be developed into networks of coupled parametric resonators to study Ising machines [18–21].

Here, we present a study of the parametric phase states of a nanomechanical resonator based on few-layer graphene at room temperature. We measure the amplitude and the phase of the vibrations in response to a strong parametric pump combined with a weak external drive. We observe a double hysteresis in both responses as ω_0 is detuned with a dc gate voltage. The double hysteresis allows us to control the phase of the parametric states. In the presence of an electrostatic force noise, the system is activated to jump between the states. We tune the stationary populations of these states by varying the phase difference between the pump and the external drive, the amplitude of the external drive, and the noise intensity. Our study is motivated by earlier works on the breaking of phase symmetry in parametric resonators based on nanobeams [9], guitar strings [22], electrical resonators [25], levitated nanoparticles [24], and torsional resonators [10]. Our results contribute to this topic and demonstrate the breaking of the symmetry of the parametric phase states in graphene. They represent a first step towards the realization of more complex systems based on coupled graphene parametric resonators, whose phase states may be mapped to a system of Ising spins.

Our nanomechanical resonator is a doubly-clamped, few-layer graphene flake shaped as a ribbon and suspended across a $3\ \mu\text{m}$ wide trench etched in silicon dioxide. A local gate electrode is patterned at the bottom of the trench (see Fig. 1a for a schematic). The device is so designed that the vertical distance between the flake and the top surface of the gate electrode is 225 nm. Flexural vibrations of the flake are driven by applying a dc voltage V_g^{dc} and an oscillating voltage $\delta V_g = A_1 \cos(\omega_d t + \theta) + A_2 \cos(2\omega_d t)$ between the gate and the flake, where $A_{1,2}$ are peak voltage amplitudes at the gate (accounting for the full reflection of the waveform at the gate). The term at ω_d in δV_g is an external drive applied near the resonant frequency ω_0 of the fundamental vibration mode. It creates a capacitive driving force of amplitude $F_d \simeq C'_g V_g^{\text{dc}} A_1$, where C'_g is the derivative of the capacitance C_g between the resonator and the gate with respect to the static displacement of the resonator. The term at $2\omega_d$ is a parametric pump [5]. It leads to an effective modulation of the spring constant via three-wave mixing of the pump at 2ω and the vibrations near ω_0 in the presence of a nonlinear restoring force [8]. The phase difference between the external drive and the pump is θ .

Our measurement setup is schematically depicted in Fig. 1a. The resonator is placed in an optical standing wave formed between the gate electrode and a quarter-wave plate.

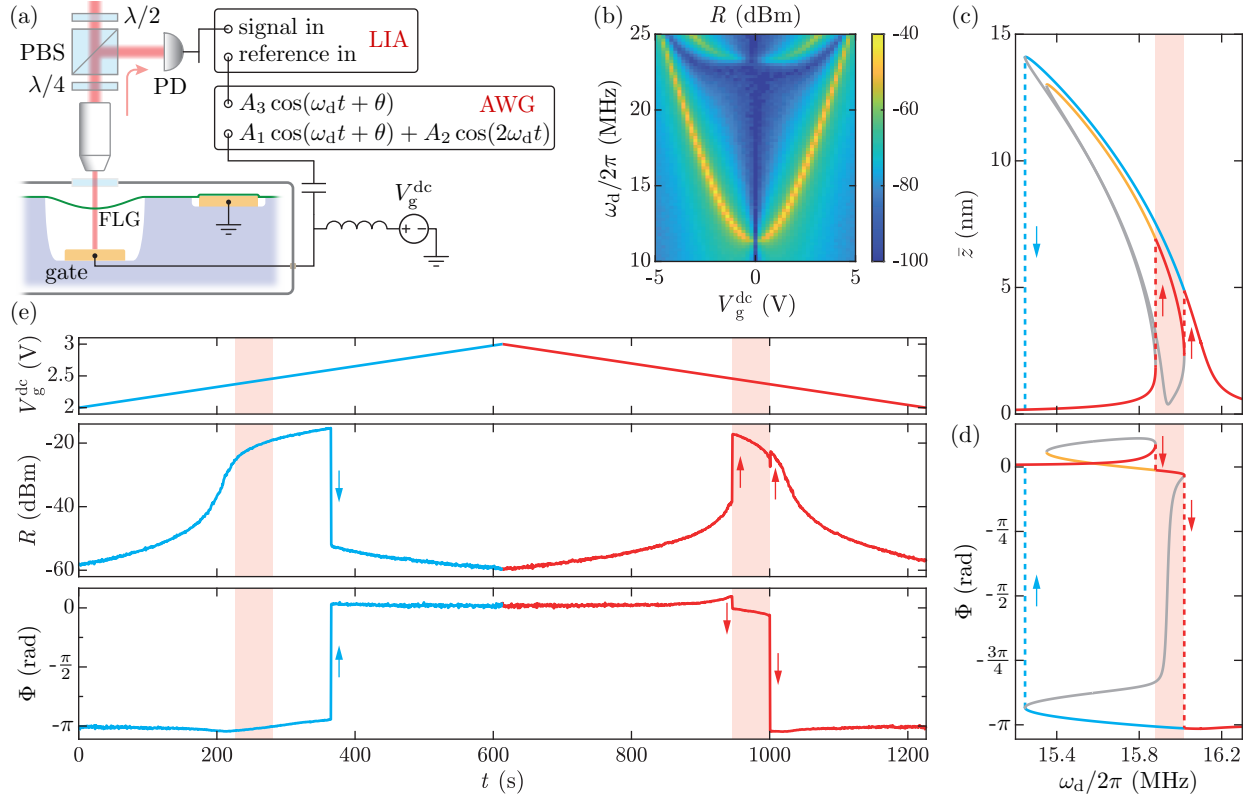


FIG. 1. Large-amplitude parametric oscillations in a graphene nanomechanical resonator. (a) Measurement setup. PD: photodetector. PBS: polarizing beam splitter. $\lambda/2$, $\lambda/4$: half-wave, quarter-wave plate. FLG: few-layer graphene. LIA: lock-in amplifier. AWG: arbitrary waveform generator. The resonator is kept in vacuum and at room temperature. A laser beam with wavelength 633 nm is used. (b) Amplitude response of the resonator measured as an electrical power R at the output of the photodetector as a function of drive frequency ω_d and gate voltage V_g^{dc} . No parametric pump is applied. The power of the external drive applied to the gate is -37 dBm. (c) Amplitude response \bar{z} and (d) phase response Φ of the stationary vibrations calculated as a function of ω_d by solving Eq. (7) with $V_g^{\text{dc}} = 2.4$ V, $A_1 = 4.2 \times 10^{-3}$ V, $A_2 = 0.635$ V, $\lambda = 0.0465$, $\theta = 125^\circ$, and the equation parameters listed in the text. Red, blue and orange traces depict stable states, while grey traces represent unstable states. The shaded region highlights the double hysteresis regime. Dotted lines and arrows indicate jumps upon changing ω_d . (e) R and Φ measured at the output of the photodetector as V_g^{dc} is increased (blue traces) and decreased (red traces). A trace with a certain color corresponds to the calculated branch with the same color in (c, d). Instead of changing ω_d , we change the resonant frequency ω_0 with V_g^{dc} . The double hysteresis is highlighted by the shaded region. A_1 , A_2 , λ , and θ are the same as in (c, d).

The amount of optical energy the resonator absorbs is modulated as it vibrates, resulting in modulations of reflected light intensity [31, 41–44]. The latter are measured with a photodetector, whose output V_{PD} is a voltage that oscillates at the frequency of the mechanical vibrations. In turn, V_{PD} is measured with a radio frequency lock-in amplifier synchronized on a clock signal oscillating at ω_{d} (Fig. 1a). Figure 1b displays the amplitude response as a function of V_{g}^{dc} and ω_{d} with $A_2 = 0$, showing that ω_0 , identified as the frequency of the peak of the response, is tunable. All measurements are done in a vacuum of 2×10^{-6} mbar and at room temperature.

Our system can be modelled by a nonlinear equation of motion for the center of mass of the resonator actuated by the external drive and the parametric pump [9, 22, 23, 26]. The equation reads:

$$\ddot{z} + \omega_0^2 [1 - \lambda \cos(\omega_{\text{p}}t)] z + \tilde{\gamma} \dot{z} + \tilde{\alpha} z^3 + \tilde{\eta} z^2 \dot{z} = \tilde{F}_{\text{d}} \cos(\omega_{\text{d}}t + \theta), \quad (1)$$

where z is the amplitude of displacement in the flexural direction, $\tilde{\gamma} = \gamma/m_{\text{eff}}$ with γ the linear damping coefficient and m_{eff} the effective mass of the vibration mode, $\tilde{\alpha} = \alpha/m_{\text{eff}}$ with α the parameter of the nonlinear conservative restoring force, $\tilde{\eta} = \eta/m_{\text{eff}}$ with η the parameter of the nonlinear dissipative force, and $\tilde{F}_{\text{d}} = F_{\text{d}}/m_{\text{eff}}$. From the dimensions of the flake measured by atomic force microscopy, we estimate $m_{\text{eff}} \simeq 1.5 \times 10^{-16}$ kg. With the parametric pump turned off, we measure the frequency response of the resonator to the external drive. Setting $C'_{\text{g}} \simeq 2.6 \times 10^{-9}$ F m⁻¹ estimated with COMSOL and $\lambda = 0$, we fit Eq. (7) to $V_{\text{PD}}(\omega_{\text{d}}) = \kappa \bar{z}(\omega_{\text{d}})$, where \bar{z} is the steady state amplitude and κ is a linear transduction factor from meter to Volt. From this fit, we extract $\tilde{\gamma} \simeq 2.05 \times 10^6$ rad/s, $\alpha \simeq -9.5 \times 10^{14}$ kg m⁻² s⁻², and $\eta \simeq 1.3 \times 10^6$ kg m⁻² s⁻¹ (Supplementary Note I). The modulation depth λ can be quantified from the response of the resonator to the pump in the absence of an external drive, $A_1 = 0$, as [5, 7]

$$\lambda = \frac{2A_2}{A_{2,\text{th}}} \frac{\tilde{\gamma}}{\omega_0} \simeq A_2 \times 7.4 \times 10^{-2} \text{ V}^{-1}, \quad (2)$$

where $A_{2,\text{th}}$ is the threshold value of the pump amplitude beyond which a response is measured, and $\omega_0/2\pi \simeq 1.6 \times 10^7$ Hz at $V_{\text{g}}^{\text{dc}} = 2.4$ V (Supplementary Note II).

Armed with the above parameters, we solve Eq. (7) using the perturbative averaging method [22]. The calculated amplitude \bar{z} and the calculated phase Φ (with respect to the external drive) of the stationary vibrations are shown as a function of ω_{d} in Figs. 1c, d for

$A_1 = 4.2 \times 10^{-3}$ V, $A_2 = 0.635$ V, $V_g^{\text{dc}} = 2.4$ V, $\omega_0/2\pi = 1.6 \times 10^7$ Hz, and $\theta = 125^\circ$. At first sight, both responses resemble those of a nonlinear resonator in the absence of a parametric pump, with an upper amplitude branch and a lower amplitude branch that form a shark fin, as well as $\Phi \simeq 0$ below and $\Phi \simeq -\pi$ above resonance. However, the interplay of nonlinearities, external drive, and pump gives rise to additional states near resonance, which become apparent as ω_d is varied. Decreasing $\omega_d/2\pi$ from 16.2 MHz, the resonator enters the parametric regime and settles in the largest amplitude state (blue trace in Fig. 1c) with $\Phi \simeq -\pi$, until it jumps to a low amplitude state with $\Phi \simeq 0$ (vertical blue arrows in Figs. 1c, d). Upon reversing the sweep direction and increasing ω_d , the resonator jumps to an intermediate amplitude state with $\Phi \simeq 0$ (leftmost vertical red arrow in Figs. 1c, d). Past this point, decreasing ω_d again would take the resonator along the orange branches in Figs. 1c, d, where \bar{z} increases and $\Phi \simeq 0$. Alternatively, continuing to increase ω_d makes the resonator jump to the largest amplitude state with $\Phi \simeq -\pi$ (rightmost vertical red arrow in Figs. 1c, d). If ω_d is first decreased from far above resonance and then increased from far below resonance, the frequency range bound by these two jumps defines a double hysteresis that makes it possible to choose the phase of vibrations. The two phase states, represented by the two traces in red and blue within the shaded region in Figs. 1c, d, can be addressed individually, now that their phase symmetry has been broken by the weak external drive.

Guided by our calculations, we experimentally prepare the resonator in one of the two phase states. To quantify the response, we measure the power R and the phase Φ of the signal at the output of the photodetector. We define $R = 10 \log_{10}[(V_{\text{PD}}/2)^2/(2 \times 50 \times 10^{-3})]$, accounting for the output impedance of the photodetector and the input impedance of the lock-in amplifier; R is a measure of \bar{z} since $V_{\text{PD}} = \kappa\bar{z}$. Attempts at measuring R and Φ as a function of ω_d proved challenging, as ω_d could not be changed adiabatically, creating stochastic jumps in R and Φ (Supplementary Note III). Instead of sweeping ω_d , we detune the resonant frequency with V_g^{dc} to bring the resonator in and out of parametric resonance [25], having set A_1 , A_2 , λ , and θ as in Figs. 1c, d. Figure 1e shows R and Φ as V_g^{dc} is first increased and then decreased. Upon decreasing V_g^{dc} , we observe two jumps in R and two concomitant jumps in Φ . Interestingly, while the second jump in R is barely noticeable (rightmost arrow in Fig. 1e), the corresponding change in Φ is large. This is explained by our calculations, where the two vibrational states have a similarly large amplitude but a phase difference of nearly π radians [9, 22, 26]. Within the double hysteresis (highlighted

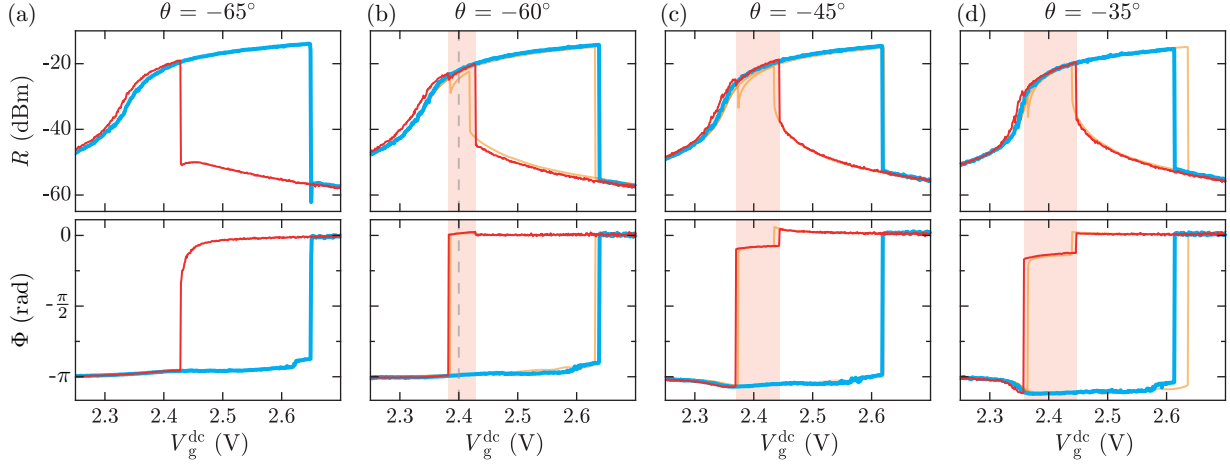


FIG. 2. Measured amplitude and phase of the output signal of the photodetector as a function of V_g^{dc} for various values of θ . A_1 , A_2 , and λ are the same as in Figs. 1c-e. Blue (red) traces: increasing (decreasing) V_g^{dc} . From (a) to (d): $\theta = -65^\circ$, -60° , -45° , -35° . Traces in orange are fits of Eq. (7) where the only fit parameter is the transduction factor κ . The vertical dashed lines in (b) indicate the state of the resonator in Fig. 3.

by the shaded regions in Fig. 1e), the phase of vibrations is controllably $\simeq 0$ (red trace in Fig. 1e) or $\simeq -\pi$ (blue trace in Fig. 1e).

As expected from Eq. (7), we find that the existence of the double hysteresis strongly depends on θ , the phase difference between the parametric pump and the external drive. Figure 2 shows R and Φ measured as a function of V_g^{dc} for several values of θ . A_1 , A_2 and λ are the same as in Figs. 1c-e. Blue (red) traces are obtained upon increasing (decreasing) V_g^{dc} . While the double hysteresis is not observed for $\theta = -65^\circ$ (Fig. 2a), it is visible for $\theta = -60^\circ$ and its width increases as θ is changed from -60° to -35° (Figs. 2b-d). However, it disappears again for $\theta = -30^\circ$ (not shown). As in Fig. 1e, the jump measured in R between the two phase states is barely detectable, while the concomitant jump in Φ is large. We can reproduce our data with the model described by Eq. (7), where the only fit parameter is the transduction factor κ .

The symmetry breaking of the phase states is also apparent in their occupation probabilities in the presence of a weak broadband force noise. This force noise is created by applying a white Gaussian voltage noise to the gate; it is quantified as an effective vibrational temperature T_{eff} using our measured thermal vibrations at room temperature as a calibration (Supplementary Note IV). Figure 3 displays Φ measured as a function of time in

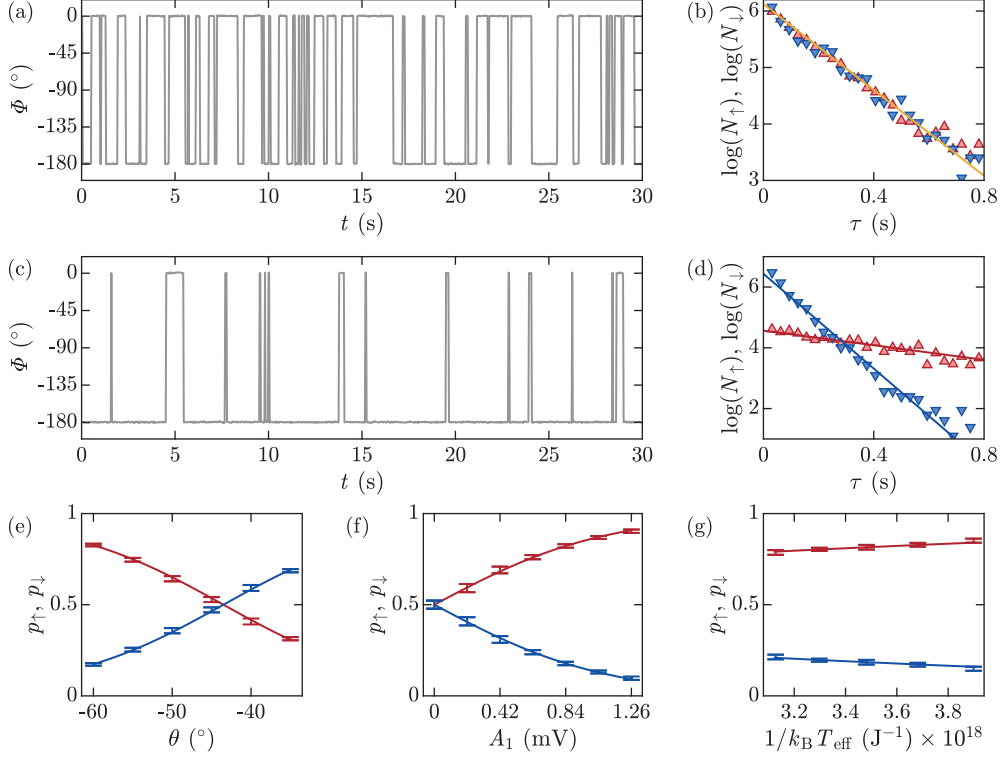


FIG. 3. Stochastic transitions and occupation probabilities of symmetry-broken parametric phase states in the presence of a white Gaussian force noise. (a) Stochastic jumps in the phase Φ of the output signal of the photodetector measured as a function of time and referenced at the input of the lock-in amplifier, with $A_1 = 0$ and $k_B T_{\text{eff}} \simeq 2.2 \times 10^{-19}$ J. (b) Distribution of the residence times τ in states \uparrow and \downarrow extracted from $\Phi(t)$ data. N_{\downarrow} are the number of transitions out of state \downarrow (red markers); N_{\uparrow} are the number of transitions out of state \uparrow (blue markers). The yellow trace is a fit of the Poisson distribution. (c) Stochastic jumps in Φ measured with $A_1 = 1.05 \times 10^{-3}$ V, $\theta = -60^\circ$, and $k_B T_{\text{eff}} \simeq 2.2 \times 10^{-19}$ J. (d) Distribution of τ in states \uparrow and \downarrow extracted from $\Phi(t)$ data. Blue and red traces are fits of the Poisson distribution to the data. (e-g) Stationary occupation probabilities p_{\downarrow} and p_{\uparrow} of states \downarrow and \uparrow as a function of θ (with $A_1 = 1.05 \times 10^{-3}$ V and $k_B T_{\text{eff}} \simeq 2.6 \times 10^{-19}$ J), A_1 (with $\theta = -60^\circ$ and $k_B T_{\text{eff}} \simeq 2.2 \times 10^{-19}$ J), and $1/k_B T_{\text{eff}}$ (with $A_1 = 1.05 \times 10^{-3}$ V and $\theta = -60^\circ$). Solid traces are fits of Eq. (6). Fit parameters are $\chi \simeq 1.1 \times 10^{-7}$ J N $^{-1}$ and $\delta \simeq -46.5^\circ$ in (e), $\chi \cos(\theta + \delta) \simeq -3.1 \times 10^{-8}$ J N $^{-1}$ in (f), and $\chi \cos(\theta + \delta) \simeq -3.2 \times 10^{-8}$ J N $^{-1}$ in (g). $V_g^{\text{dc}} = 2.4$ V, $\omega_0/2\pi \simeq \omega_d/2\pi = 1.6 \times 10^7$ Hz, and $A_2 = 0.635$ V in all panels.

the presence of the force noise, without applying an external drive ($A_1 = 0$). We have set $A_2 = 0.635$ V, $V_g^{\text{dc}} = 2.4$ V, and $\omega_d/2\pi = 1.6 \times 10^7$ Hz. Φ jumps stochastically between $\simeq 0$ and $\simeq -\pi$, indicating random and uncorrelated transitions between the two states [9–15]. The stationary occupation probability of each state is measured as $p_{\uparrow,\downarrow} = t_{\uparrow,\downarrow}/t_{\text{meas}}$, where \uparrow (\downarrow) labels the state with $\Phi = 0$ ($\Phi = -\pi$), t_{\uparrow} (t_{\downarrow}) is the total time spent in state \uparrow (\downarrow), and t_{meas} is the total measurement time. We find $p_{\uparrow} \simeq p_{\downarrow}$, showing that the states are degenerate, in agreement with Ref. [9]. The statistics of transitions is well described by the Poisson distribution, as shown in Fig. 3b where the number of transitions out of a given state $N_{\uparrow,\downarrow}$ is plotted as a function of the residence time τ . A fit of an exponential decay allows us to estimate the transition rates W_{\uparrow} out of state \uparrow and W_{\downarrow} out of state \downarrow , where we find $W_{\uparrow} \simeq W_{\downarrow}$. Measuring $W_{\uparrow,\downarrow}$ as a function of T_{eff} (Supplementary Note V), we verify that they follow an activation law [10–15]:

$$W_{\uparrow,\downarrow} = C \exp(-U_{\uparrow,\downarrow}/k_B T_{\text{eff}}), \quad (3)$$

with C a constant and U_{\uparrow} (U_{\downarrow}) the activation energy out of state \uparrow (\downarrow).

Applying a small external drive lifts the occupation degeneracy of the states. We prepare the resonator within the frequency range between the jumps (shaded area in Fig. 2b) using $A_1 = 1.05 \times 10^{-3}$ V and $\theta = -60^\circ$ (vertical dashed lines in Fig. 2b). Φ displays jumps that favor state \downarrow (Fig. 3c). Accordingly, the statistics of the transitions reveals that $W_{\downarrow} \ll W_{\uparrow}$ (Fig. 3d). We then measure the occupation probabilities of the two states as a function of θ and A_1 , the parameters of the symmetry-breaking drive. With $A_1 = 1.05 \times 10^{-3}$ V, p_{\uparrow} and p_{\downarrow} show a clear dependence on θ (Fig. 3e). Similarly, with $\theta = -60^\circ$, p_{\uparrow} and p_{\downarrow} strongly vary with A_1 (Fig. 3f). Both behaviors can be explained by the change in transition rates caused by the external drive $F_d \cos(\omega_d t + \theta)$. According to the theory in Ref. [23], the external drive modifies the activation energies as

$$U_{\uparrow,\downarrow} = \bar{U} + \sigma_{\uparrow,\downarrow} \chi F_d \cos(\theta + \delta), \quad (4)$$

where \bar{U} is the activation energy in the absence of a symmetry breaking drive, $\sigma_{\uparrow} = 1$, $\sigma_{\downarrow} = -1$, and χ and δ are the magnitude and the phase of the logarithmic susceptibility of the resonator. Expressing $p_{\uparrow,\downarrow}$ as the stationary solutions to the balance equation for the occupation probabilities,

$$p_{\uparrow,\downarrow} = \frac{W_{\downarrow,\uparrow}}{W_{\uparrow} + W_{\downarrow}}, \quad (5)$$

Eqs. (10) and (11) yield [10]

$$p_{\uparrow,\downarrow} = \left\{ 1 + \exp \left[\frac{-2\sigma_{\uparrow,\downarrow}\chi F_d \cos(\theta + \delta)}{k_B T_{\text{eff}}} \right] \right\}^{-1}. \quad (6)$$

We fit Eq. (6) to our measurements in Figs. 3e, f (solid traces), using χ and δ as fit parameters. With $A_1 = 1.05 \times 10^{-3}$ V and $\theta = -60^\circ$, we also measure $p_{\uparrow,\downarrow}$ as a function of $1/k_B T_{\text{eff}}$, and fit Eq. (6) to the data in Fig. 3g. Measurements of the logarithmic susceptibility are presented in Supplementary Note VI. In Supplementary Note VII, we present additional measurements obtained with a second few-layer graphene resonator, reproduce our analysis, and obtain results similar to those presented here.

We have demonstrated that parametric phase states with broken symmetry can be created in nanomechanical resonators made from graphene. This paves the way towards the realization of phase logic devices with a combination of useful properties. (i) Our resonator has a footprint of a few squared micrometers, which allows massive parallel implementation on a single chip. (ii) Graphene resonators have a low mass, and can therefore be driven with low power. (iii) Our device has a bandwidth of about 1 MHz, which should make it possible to flip the phase states within a few microseconds using optimized protocols. (iv) Graphene resonators can be tuned over a wide frequency range with electrical gates. Such tuning is not only important to obtain resonant coupling between neighboring devices, but, as we show here, provides a toolbox for flipping the phase states of individual devices in a deterministic manner. Summarizing the above properties, we have all the ingredients for realizing large on-chip networks of highly tunable parametric oscillators. Such networks could become a resource for solving complex optimization tasks, such as the travelling salesman problem or finding the ground state of an Ising Hamiltonian. The combination of small size, low power, high bandwidth, and frequency tuning and phase flipping via gate electrodes makes graphene resonators a promising platform for this endeavor.

Future work will focus on the performance of coupled devices. On the one hand, we hope that the complexity of operating coupled parametric oscillators can be reduced with the gate switching method shown here. On the other hand, we will investigate various algorithms to perform optimization tasks based on various proposals, and will compare their results. Because the two nearly symmetrical phase states of a parametric oscillator can be mapped to a two-level system, weakly coupled parametric oscillations can be mapped to a system of Ising spins [18–21]. These systems have attracted renewed interest in the

context of machine learning [45–47]. The coupling between parametric oscillators has the same effect on transition rates as a weak external drive [10] and breaks phase symmetry. While nominally identical nanomechanical resonators often display non-identical vibrational resonant frequencies due to fabrication challenges, the variability of resonant frequencies may serve as a way to realize weak disorder in a coupled array of such resonators. The array can then be mapped to an asymmetric Ising system [48–51] featuring unusual out-of-equilibrium phenomena, such as a nonzero probability current among the stationary populations of the parametric states [10].

ACKNOWLEDGMENTS

This work was supported by the National Natural Science Foundation of China (grant numbers 62150710547 and 62074107) and the project of the Priority Academic Program Development (PAPD) of Jiangsu Higher Education Institutions. The authors are grateful to Prof. Wang Chinhua for his strong support. J.M. is grateful to Antoine Reserbat-Plantey and Fabien Violla for inspiring discussions.

SUPPLEMENTARY INFORMATION

A. Estimating the parameters of the equation of motion

In the absence of a parametric pump, $\lambda = 0$, the equation of motion for the steady-state displacement of the center of mass of the resonator reads:

$$\rho^3 \left[\frac{9}{16} \tilde{\alpha}^2 + \frac{1}{16} \tilde{\eta}^2 \omega_d^2 \right] + \rho^2 \left[-\frac{3}{2} \tilde{\alpha} (\omega_d^2 - \omega_0^2) + \frac{1}{2} \tilde{\eta} \tilde{\gamma} \omega_d^2 \right] + \rho \left[(\omega_d^2 - \omega_0^2)^2 + \tilde{\gamma}^2 \omega_d^2 \right] - \tilde{F}_d^2 = 0, \quad (7)$$

where $\rho = \bar{z}^2$, with \bar{z} the steady-state amplitude of displacement, and where $\tilde{\alpha} = \alpha/m_{\text{eff}}$, $\tilde{\eta} = \eta/m_{\text{eff}}$, $\tilde{\gamma} = \gamma/m_{\text{eff}}$, $\tilde{F}_d = F_d/m_{\text{eff}}$, and $\omega_d = 2\pi f_d$. α is the parameter of the nonlinear conservative restoring force, η is the parameter of the nonlinear dissipative force, γ is the linear damping coefficient, m_{eff} is the effective masse of the vibration mode, ω_0 is the angular resonant frequency, and F_d and ω_d are the amplitude and the angular frequency of the external drive, respectively.

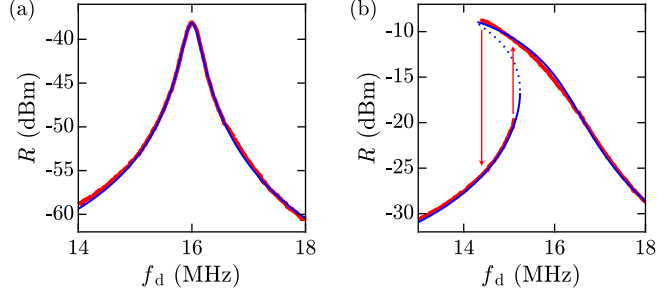


FIG. 4. Estimating the parameters of the equation of motion. Red traces are measured data and blue traces are fits of Eq. (7) [blue dots indicate unstable solutions]. (a) Linear response. $F_d \simeq 2.8 \times 10^{-11}$ N; $P_{\text{inc}} \simeq 15.5 \times 10^{-6}$ W. (b) Nonlinear response. $F_d \simeq 8.9 \times 10^{-10}$ N; $P_{\text{inc}} \simeq 19 \times 10^{-6}$ W. In (a) and (b), $V_g^{\text{dc}} = 2.4$ V, $G = 2.5 \times 10^5$ V W $^{-1}$; $T \simeq 0.5$; $|\partial r / \partial z_s| \simeq 4.5 \times 10^{-3}$ nm $^{-1}$.

We consider Resonator A in the main text and measure the power R of the signal at the output of the photodetector as a function of the drive frequency f_d . Labeling the output peak voltage of the photodetector as V_{PD} , the power in units of dBm that is dissipated across the input impedance of our lock-in amplifier reads $R = 10 \log_{10}[(V_{\text{PD}}/2)^2/(2 \times 50 \times 10^{-3})]$, where one factor of $1/2$ accounts for the rms averaging of the voltage and the other one accounts for the voltage divider that originates from the output impedance of the photodetector and the input impedance of the lock-in amplifier. Our vibration detection scheme is linear, $V_{\text{PD}} = \kappa \bar{z}$, with $\kappa = P_{\text{inc}} \times T \times G \times |\partial r / \partial z_s|$ a transduction factor from meter to Volt; P_{inc} is the optical power incident on the resonator, T is the transmittance of the optical path from the resonator to the photodetector, G is the transimpedance gain of the photodetector, and $\partial r / \partial z_s$ is the derivative with respect to the static displacement of the resonator z_s of the optical reflection coefficient r at the surface of the resonator facing the light source. The amplitude of the external drive reads $F_d \simeq C'_g V_g^{\text{dc}} \delta V_g$, where V_g^{dc} and δV_g are the dc voltage and the peak amplitude of the oscillating voltage applied between the gate and the resonator, respectively, and $C'_g = \partial C_g / \partial z_s$ is the derivative of the capacitance between the gate and the resonator. δV_g accounts for the full reflection of the voltage wave at the gate, hence δV_g is twice the amplitude of the voltage wave incident on the gate. The power of the voltage wave driving the resonator that would be dissipated across a 50 Ohm resistor is $P_d = 10 \log_{10}[\delta V_g^2/(2 \times 50 \times 10^{-3})]$ in units of dBm, where the factor of $1/2$ accounts for the rms averaging of the voltage. We estimate $C'_g \simeq 2.6 \times 10^{-9}$ F m $^{-1}$ using COMSOL. Finally, we estimate $m_{\text{eff}} \simeq 1.5 \times 10^{-16}$ kg from atomic force microscopy images of the few-layer

graphene membrane.

Figure 4a shows $R(f_d)$ in response to a weak drive, for which the response is linear. Fitting Eq. (7) to our measured data, we estimate $\tilde{\gamma} \simeq 2.05 \times 10^6 \text{ rad s}^{-1}$. Figure 4b shows $R(f_d)$ in response to a larger drive, for which the response is nonlinear. Fitting Eq. (7) to the data, we estimate $\alpha \simeq -9.5 \times 10^{14} \text{ kg m}^{-2} \text{ s}^{-2}$ and $\eta \simeq 1.3 \times 10^6 \text{ kg m}^{-2} \text{ s}^{-1}$.

B. Estimating the parametric modulation depth λ

Applying a parametric pump voltage $A_2 \cos(2\omega_d t)$ with $\omega_d \simeq \omega_0$, where ω_0 is the angular resonant frequency, effectively modulates the spring constant of the resonator. The modulation depth λ can be estimated from the response of the resonator to the pump in the absence of an external drive, $F_d = 0$, as [5, 7]

$$\lambda = \frac{2A_2 \tilde{\gamma}}{A_{2,\text{th}} \omega_0}, \quad (8)$$

where $A_{2,\text{th}}$ is the threshold value of the pump amplitude beyond which a response is measured.

We consider Resonator A in the main text. Figure 5 shows the power of the signal at the output of the photodetector R [see Supplementary Note 1 for the definition of R] as a function of A_2 upon increasing (Fig. 5a) and decreasing (Fig. 5b) $f_d = \omega_d/2\pi$. We have set $V_g^{\text{dc}} = 2.4 \text{ V}$, yielding $\omega_0/2\pi \simeq 1.6 \times 10^7 \text{ Hz}$. We find that R becomes measurable above $A_{2,\text{th}} \simeq 0.555 \text{ V}$. Hence we estimate $\lambda \simeq A_2 \times 7.4 \times 10^{-2} \text{ V}^{-1}$.

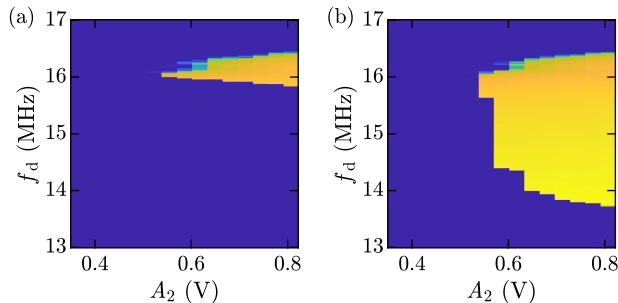


FIG. 5. Estimating the parametric modulation depth λ . A pump voltage $A_2 \cos(2 \times 2\pi f_d t)$ is applied between the resonator and the gate. The power of the signal at the output of the photodetector R is shown as a function of A_2 upon increasing (a) and decreasing (b) f_d . Power scale: blue, -80 dBm ; yellow, -6 dBm .

C. Stochastic frequency jumps upon changing f_d

We measured a second device, labeled as Device B, at a cryostat temperature of 3 K. A two-source mixing technique was used to measure vibrations, instead of the optical technique employed in the main text and elsewhere in these Supplementary Notes. Figure 6a depicts the amplitude of the electromechanical mixing current I_{mix} in the linear regime as a function of the gate voltage V_g^{dc} and of the drive frequency f_d , in the absence of a parametric pump, showing that the resonant frequency is still tunable at low temperature. With the compound excitation $\delta V_g = A_1 \cos(2\pi f_d t + \theta) + A_2 \cos(2 \times 2\pi f_d t)$ applied between the gate and the resonator, attempts at measuring I_{mix} and the phase of the mixing current Φ as a function of f_d proved challenging. f_d could not be changed adiabatically, creating stochastic jumps in I_{mix} and in Φ . Figures 6b and 6c show I_{mix} and Φ , respectively, as f_d is being incremented and then decremented by small steps. Stochastic jumps are observed in both responses. However, it is still possible to fit Eq. (1) in the main text to the data, revealing the double hysteresis that signals the breaking of the symmetry of the parametric phase states.

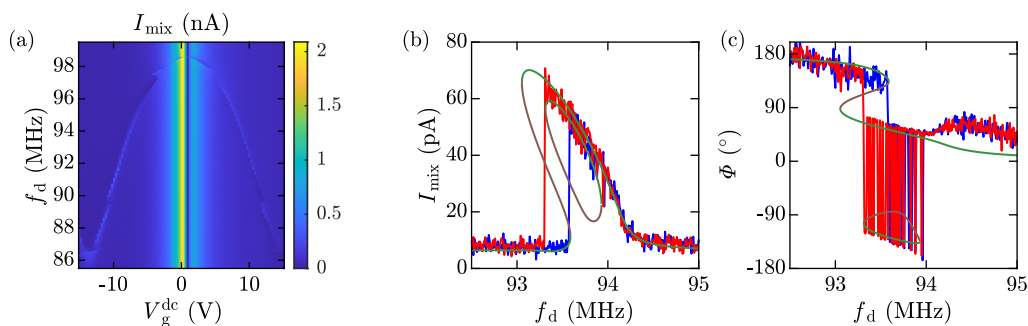


FIG. 6. Stochastic frequency jumps upon changing f_d at 3 K. A two-source mixing technique is used to measure vibrations. (a) Amplitude of the mixing current I_{mix} at the drain electrode of the resonator as a function of gate voltage V_g^{dc} and drive frequency f_d in the absence of a parametric pump. $A_1 = 8.5 \times 10^{-3}$ V. (b) I_{mix} and (c) phase of the mixing current Φ upon incrementing (blue traces) and decrementing (red traces) f_d . $V_g^{\text{dc}} = -8$ V; $A_1 = 7 \times 10^{-3}$ V; $A_2 = 0.05$ V; $\theta = 0^\circ$. The green traces are stable solutions of Eq. (1) in the main text, while the brown traces are unstable solutions. The data analysis is based on $m_{\text{eff}} \simeq 3 \times 10^{-17}$ kg, $\tilde{\gamma} \simeq 2.96 \times 10^5$ rad s $^{-1}$, $\alpha \simeq -2.4 \times 10^{17}$ kg m $^{-2}$ s $^{-2}$, and $\eta \simeq 3.2 \times 10^8$ kg m $^{-2}$ s $^{-1}$.

D. Calibrating the force noise

We submit Resonator A in the main text to a force noise by applying a white Gaussian voltage noise between the resonator and the gate. We quantify the force noise as an effective vibrational temperature T_{eff} using thermal vibrations measured at room temperature as a calibration (Figs. 7a, b),

$$T_{\text{eff}}(\xi^2) = \frac{\sigma^2(\xi^2)}{\sigma^2(\xi^2 = 0)} \times 300 \text{ K}, \quad (9)$$

where ξ^2 is the variance of the voltage noise and σ^2 is the area under the power spectral density of voltage fluctuations S_{vv} at the output of the photodetector.

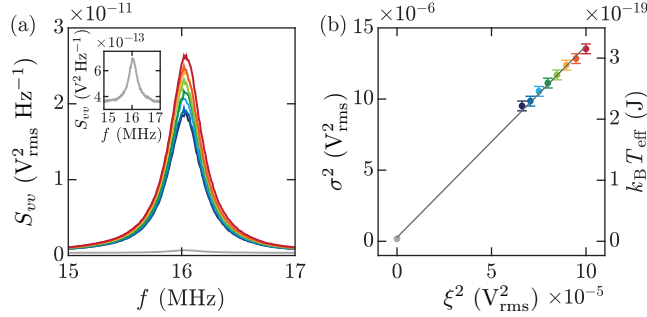


FIG. 7. Calibrating the force noise. (a) Power spectral density of voltage fluctuations S_{vv} at the output of the photodetector as a function of spectral frequency f for various variances ξ^2 of the white Gaussian voltage noise applied between the resonator and the gate. From dark blue (bottom trace) to dark red (top trace), ξ^2 increases from 6.6×10^{-5} to $10^{-4} \text{ V}_{\text{rms}}^2$. $S_{vv}(f)$ at room temperature is shown as the grey trace in this panel and in the inset. (b) Left-hand-side ordinate axis: area under $S_{vv}(f)$, σ^2 , as a function of ξ^2 . Right-hand-side ordinate axis: effective thermal energy $k_{\text{B}}T_{\text{eff}}$, with k_{B} the Boltzmann constant. The straight line is a linear fit. A spectrum in (a) and its corresponding dot in (b) have the same color.

E. Activation of the transition rates between the two parametric phase states

We consider Resonator A in the main text. Figure 8 shows the transition rates W_{\uparrow} out of state \uparrow and W_{\downarrow} out of state \downarrow , where \uparrow (\downarrow) labels the phase state with $\Phi = 0$ ($\Phi = -\pi$), as a function of the effective thermal energy $k_{\text{B}}T_{\text{eff}}$ induced by a white Gaussian force noise (Supplementary Note D). A parametric pump of amplitude $A_2 = 0.635 \text{ V}$ is applied in the

absence of an external drive ($A_1 = 0$). We find that $W_\uparrow \simeq W_\downarrow$. We also find that $W_{\uparrow,\downarrow}$ follow an activation law [10–15]:

$$W_{\uparrow,\downarrow} = C \exp(-U_{\uparrow,\downarrow}/k_B T_{\text{eff}}) , \quad (10)$$

with C a constant and U_\uparrow (U_\downarrow) the activation energy out of state \uparrow (\downarrow). A fit of Eq. (10) to the data yields $U_\uparrow \simeq U_\downarrow \simeq 3.6 \times 10^{-18}$ J.

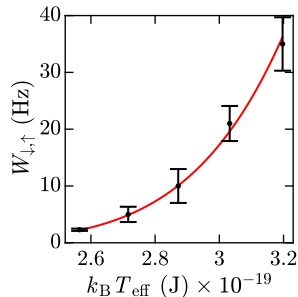


FIG. 8. Activation of the transition rates $W_{\uparrow,\downarrow}$ between the two parametric phase states. $W_{\uparrow,\downarrow}$ measured as a function of the effective thermal energy $k_B T_{\text{eff}}$ with $A_1 = 0$ and $A_2 = 0.635$ V.

F. Measuring the logarithmic susceptibility

According to the theory in Ref. [23], the external drive $F_d \cos(\omega_d t + \theta)$ modifies the activation energies $U_{\uparrow,\downarrow}$ (see Supplementary Note E) as

$$U_{\uparrow,\downarrow} = \bar{U} + \sigma_{\uparrow,\downarrow} \chi F_d \cos(\theta + \delta) , \quad (11)$$

where \bar{U} is the activation energy in the absence of a symmetry breaking drive ($F_d = 0$), $\sigma_\uparrow = 1$, $\sigma_\downarrow = -1$, and χ and δ are the magnitude and the phase of the logarithmic susceptibility of the resonator.

The logarithmic susceptibility can be extracted from the ratio of the transition rates W_\downarrow/W_\uparrow . Indeed, combining Eqs. (10) and (11) yields

$$\log\left(\frac{W_\downarrow}{W_\uparrow}\right) = \frac{2\chi F_d \cos(\theta + \delta)}{k_B T_{\text{eff}}} . \quad (12)$$

We consider Resonator A in the main text. In Figs. 9a-c, we measure $\log(W_\downarrow/W_\uparrow)$ as a function of A_1 (with $\theta = -60^\circ$ and $k_B T_{\text{eff}} \simeq 2.2 \times 10^{-19}$ J), θ (with $A_1 = 1.05 \times 10^{-3}$ V and $k_B T_{\text{eff}} \simeq 2.6 \times 10^{-19}$ J), and $1/k_B T_{\text{eff}}$ ($A_1 = 1.05 \times 10^{-3}$ V and $\theta = -60^\circ$), all with $V_g^{\text{dc}} = 2.4$ V,

$A_2 = 0.635$ V, and $\omega_0/2\pi \simeq \omega_d/2\pi = 1.6 \times 10^7$ Hz. Fitting Eq. (12) to these data, we find similar values for the logarithmic susceptibility: $\chi \cos(\theta + \delta) \simeq -3.1 \times 10^{-8}$ J N $^{-1}$ (Figs. 9a, c), and $\chi \simeq 1.1 \times 10^{-7}$ J N $^{-1}$ and $\delta \simeq -46.5^\circ$ (Fig. 9b).

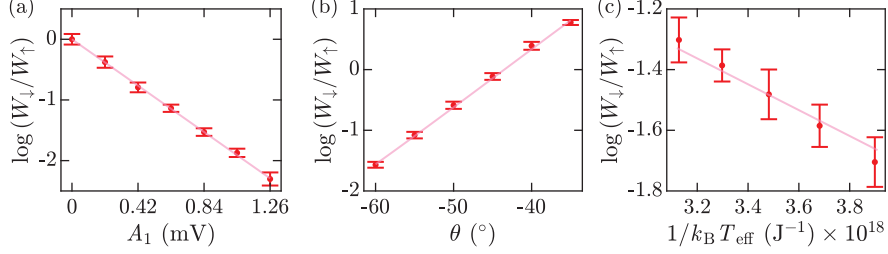


FIG. 9. Measuring the logarithmic susceptibility. (a) Natural logarithm of the ratio of the transition rates, $\log(W_{\downarrow}/W_{\uparrow})$, as a function of A_1 with $\theta = -60^\circ$ and $k_B T_{\text{eff}} \simeq 2.2 \times 10^{-19}$ J. The solid trace is a fit of the data to Eq. (12) with $\chi \cos(\theta + \delta) \simeq -3.1 \times 10^{-8}$ J N $^{-1}$. (b) $\log(W_{\downarrow}/W_{\uparrow})$ as a function of θ with $A_1 = 1.05 \times 10^{-3}$ V and $k_B T_{\text{eff}} \simeq 2.6 \times 10^{-19}$ J. The solid trace is a fit of Eq. (12) with $\chi \simeq 1.1 \times 10^{-7}$ J N $^{-1}$ and $\delta \simeq -46.5^\circ$. (c) $\log(W_{\downarrow}/W_{\uparrow})$ as a function of $1/k_B T_{\text{eff}}$ with $A_1 = 1.05 \times 10^{-3}$ V and $\theta = -60^\circ$. The solid trace is a fit of Eq. (12) with $\chi \cos(\theta + \delta) \simeq -3.2 \times 10^{-8}$ J N $^{-1}$. $V_g^{\text{dc}} = 2.4$ V, $\omega_0/2\pi \simeq \omega_d/2\pi = 1.6 \times 10^7$ Hz, and $A_2 = 0.635$ V in all panels.

G. Parametric phase states measured in Resonator C

We studied the parametric phase state of a third device, Resonator C. This device had the same structure and geometry as Resonator A in the main text. We estimated the effective mass of the fundamental mode to be $m_{\text{eff}} \simeq 7.2 \times 10^{-16}$ kg. Measurements were performed optically, with the resonator at room temperature and in vacuum, as with Resonator A in the main text.

Figure 10a shows the power R of the signal at the output of the photodetector in the linear regime as a function of the gate voltage V_g^{dc} and of the drive frequency f_d , in the absence of a parametric pump. (See Supplementary Note A for the definition of R .) Figure 10b shows $R(f_d)$ measured in the linear regime. A fit of a Lorentzian lineshape allows us to estimate the damping rate $\tilde{\gamma} \simeq 1.3 \times 10^6 \text{ rad s}^{-1}$. Figure 10c shows $R(f_d)$ measured in the nonlinear regime. A fit of the nonlinear response allows us to estimate the parameter of the nonlinear restoring force $\alpha \simeq -1.35 \times 10^{17} \text{ kg m}^{-2} \text{ s}^{-2}$ and the parameter of the nonlinear dissipative force $\eta \simeq 6 \times 10^8 \text{ kg m}^{-2} \text{ s}^{-1}$.

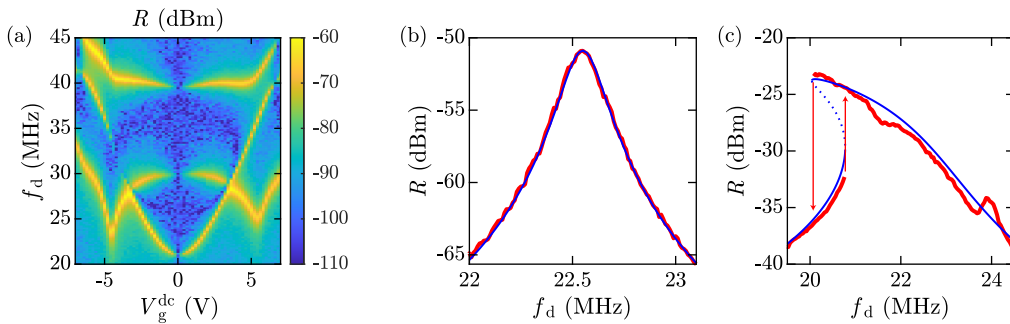


FIG. 10. Response of Resonator C to an external drive. (a) Amplitude response R as a function of drive frequency f_d and gate voltage V_g^{dc} in the absence of a parametric pump. The power of the external drive applied between the resonator and the gate is $P_d = -37 \text{ dBm}$. (b) Linear response at $V_g^{\text{dc}} = 1.6 \text{ V}$ and $P_d = -33 \text{ dBm}$ ($F_d \simeq 3 \times 10^{-11} \text{ N}$). Optical power incident on the resonator, $P_{\text{inc}} \simeq 14.1 \times 10^{-6} \text{ W}$. (c) Nonlinear response at $V_g^{\text{dc}} = 1.6 \text{ V}$ and $P_d = 7 \text{ dBm}$ ($F_d \simeq 3 \times 10^{-9} \text{ N}$). $P_{\text{inc}} \simeq 14.7 \times 10^{-6} \text{ W}$. In (a) and (b), the red traces are measured data and the blue traces are fits of Eq. (7). $G = 2.5 \times 10^5 \text{ V W}^{-1}$, $T \simeq 0.5$, and $|\partial r / \partial z_s| \simeq 4.5 \times 10^{-3} \text{ nm}^{-1}$ in all panels.

Figure 11 shows R and the phase Φ of the signal at the output of the photodetector as a function of V_g^{dc} for several values of the phase angle θ of the external drive. Φ is measured at the input of the lock-in amplifier. We apply a compound excitation $\delta V_g = A_1 \cos(2\pi f_d t + \theta) + A_2 \cos(2 \times 2\pi f_d t)$ between the gate and the resonator, with $A_1 = 1.4 \times 10^{-2} \text{ V}$, $A_2 = 1.26 \text{ V}$, and $f_d = 2.26 \times 10^7 \text{ Hz}$. The blue (red) traces are obtained by increasing (decreasing) V_g^{dc} . The double hysteresis is not found for $\theta = -80^\circ$ but is observed for θ ranging from -75° to -20° . It disappears again for $\theta = -15^\circ$ (not shown).

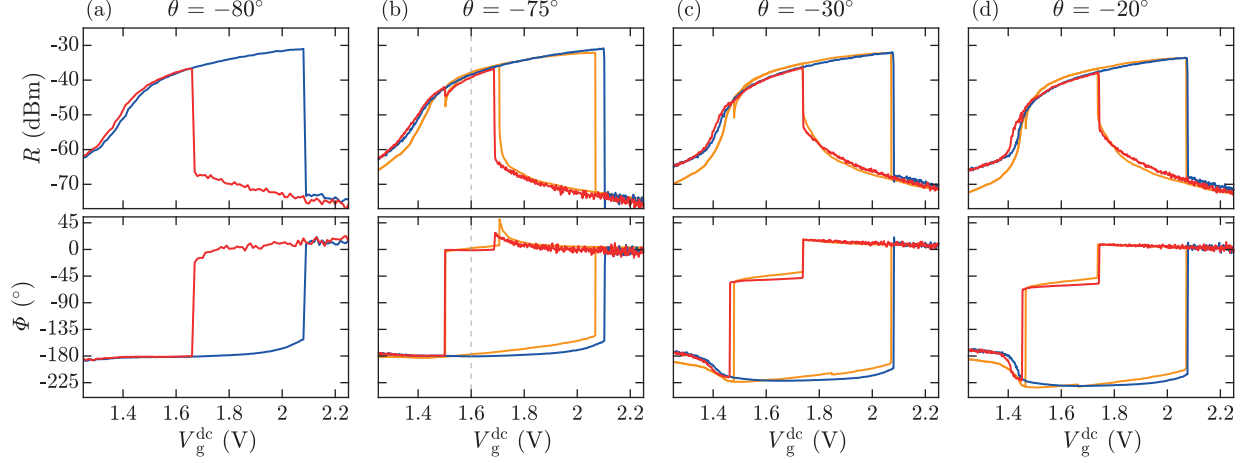


FIG. 11. Amplitude and phase of the signal at the output of the photodetector as a function of V_g^{dc} for various values of the phase angle θ of the external drive (Resonator C). $A_1 = 1.4 \times 10^{-2}$ V, $A_2 = 1.26$ V, $\lambda \simeq 0.05$, and $f_d = 2.26 \times 10^7$ Hz. The blue (red) traces are obtained upon increasing (decreasing) V_g^{dc} . From (a) to (d), $\theta = -80^\circ$, -75° , -30° , and -20° . The orange traces are fits of Eq. (1) in the main text with the transduction factor κ as a fit parameter. The vertical dashed lines in (b) show the state of the resonator in Figs. 12 and 13.

Figure 12 shows the measured occupation probabilities $p_{\uparrow,\downarrow}$ of the two parametric phase states in the presence of a white Gaussian force noise. Figure 12a shows $p_{\uparrow,\downarrow}$ as a function of θ . Figure 12b shows $p_{\uparrow,\downarrow}$ as a function of A_1 . Figure 12c shows $p_{\uparrow,\downarrow}$ as a function of $1/k_B T_{\text{eff}}$.

Figure 13 shows the natural logarithm of the ratio of the measured transition rates $W_{\uparrow,\downarrow}$ as a function of A_1 , θ , and $1/k_B T_{\text{eff}}$. We employ $\log[W_{\downarrow}/W_{\uparrow}]$ to estimate the logarithmic susceptibility of the resonator (see Supplementary Note F).

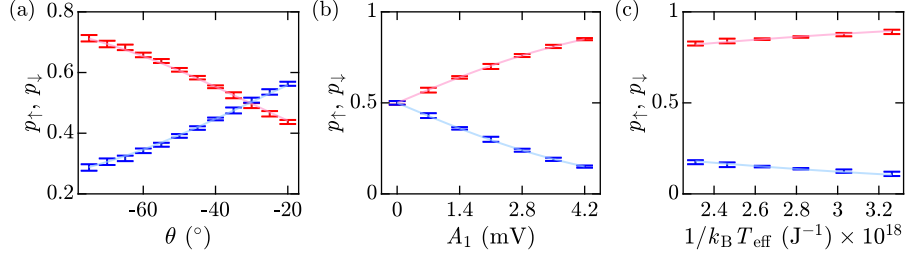


FIG. 12. Occupation probabilities $p_{\uparrow, \downarrow}$ of the parametric phase states in the presence of a white Gaussian force noise (Resonator C). (a) $p_{\uparrow, \downarrow}$ as a function of θ with $A_1 = 1.4 \times 10^{-3}$ V and $k_B T_{\text{eff}} \simeq 3.7 \times 10^{-19}$ J. (b) $p_{\uparrow, \downarrow}$ as a function of A_1 with $\theta = -75^\circ$ and $k_B T_{\text{eff}} \simeq 6.1 \times 10^{-19}$ J. (c) $p_{\uparrow, \downarrow}$ as a function of $1/k_B T_{\text{eff}}$ with $A_1 = 2.8 \times 10^{-3}$ V and $\theta = -75^\circ$. Solid traces are fits of Eq. (6) in the main text. Fit parameters are (a) $\chi \simeq 4 \times 10^{-8}$ J N $^{-1}$, $\delta \simeq -59.5^\circ$; (b) $\chi \cos(\theta + \delta) \simeq -3 \times 10^{-8}$ J N $^{-1}$; (c) $\chi \cos(\theta + \delta) \simeq -2.8 \times 10^{-8}$ J N $^{-1}$. In all panels, $V_g^{\text{dc}} = 1.6$ V, $A_2 = 1.26$ V, and $f_d = 2.26 \times 10^7$ Hz.

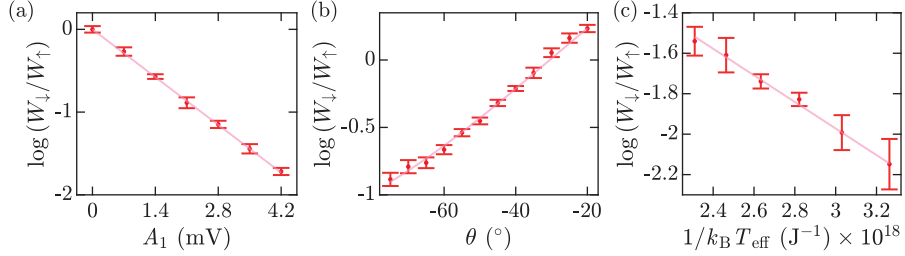


FIG. 13. Logarithmic susceptibility of Resonator C. (a) $\log[W_{\downarrow}/W_{\uparrow}]$ as a function of A_1 with $\theta = -75^\circ$ and $k_B T_{\text{eff}} \simeq 6.1 \times 10^{-19}$ J. The solid trace is a fit of Eq. (12) with $\chi \cos(\theta + \delta) \simeq -3 \times 10^{-8}$ J N $^{-1}$. (b) $\log[W_{\downarrow}/W_{\uparrow}]$ as a function of θ with $A_1 = 1.4 \times 10^{-3}$ V and $k_B T_{\text{eff}} \simeq 3.7 \times 10^{-19}$ J. The solid trace is a fit of Eq. (12) with $\chi \simeq 4 \times 10^{-8}$ J N $^{-1}$ and $\delta \simeq -59.5^\circ$. (c) $\log[W_{\downarrow}/W_{\uparrow}]$ as a function of $1/k_B T_{\text{eff}}$ with $A_1 = 2.8 \times 10^{-3}$ V and $\theta = -75^\circ$. The solid trace is a fit of Eq. (12) with $\chi \cos(\theta + \delta) \simeq -2.8 \times 10^{-8}$ J N $^{-1}$. In all panels, $V_g^{\text{dc}} = 1.6$ V, $A_2 = 1.26$ V, and $f_d = 2.26 \times 10^7$ Hz.

[1] D. Rugar and P. Grütter, Mechanical parametric amplification and thermomechanical noise squeezing, *Phys. Rev. Lett.* **67**, no. 6, 699–702 (1991). <https://doi.org/10.1103/PhysRevLett.67.699>

- [2] K. L. Turner, S. A. Miller, P. G. Hartwell, N. C. MacDonald, S. H. Strogatz, and S. G. Adams, Five parametric resonances in a microelectromechanical system, *Nature* **396**, no. 6707, 149–152 (1998). <https://doi.org/10.1038/24122>
- [3] D. W. Carr, S. Evoy, L. Sekaric, H. G. Craighead, and J. M. Parpia, Parametric amplification in a torsional microresonator, *Appl. Phys. Lett.* **77**, no. 10, 1545–1547 (2000). <https://doi.org/10.1063/1.1308270>
- [4] R. B. Karabalin, S. C. Masmanidis, and M. L. Roukes, Efficient parametric amplification in high and very high frequency piezoelectric nanoelectromechanical systems, *Appl. Phys. Lett.* **97**, no. 18, 183101 (2010). <https://doi.org/10.1063/1.3505500>
- [5] A. Eichler, J. Chaste, J. Moser, and A. Bachtold, Parametric amplification and self-oscillation in a carbon nanotube resonator, *Nano Lett.* **11**, no. 7, 2699–2703 (2011). <https://doi.org/10.1021/nl200950d>
- [6] J. Gieseler, B. Deutsch, R. Quidant, and L. Novotny, Subkelvin parametric feedback cooling of a laser-trapped nanoparticle, *Phys. Rev. Lett.* **109**, no. 10, 103603 (2012). <https://doi.org/10.1103/PhysRevLett.109.103603>
- [7] M. C. Lifshitz and R. Cross, Nonlinear Dynamics of Nanomechanical Resonators (2010). In *Nonlinear Dynamics of Nanosystems* (eds G. Radons, B. Rumpf and H.G. Schuster). <https://doi.org/10.1002/9783527629374.ch8>
- [8] A. Eichler and O. Zilberberg, “Classical and Quantum Parametric Phenomena”, Oxford Graduate Texts (2023). <https://academic.oup.com/book/55246>
- [9] I. Mahboob, C. Froitier, and H. Yamaguchi, A symmetry-breaking electromechanical detector, *Appl. Phys. Lett.* **96**, no. 21, 213103 (2010). <https://doi.org/10.1063/1.3429589>
- [10] C. Han, M. Wang, B. Zhang, M. I. Dykman, and H. B. Chan, Coupled parametric oscillators: From disorder-induced current to asymmetric Ising model, *Phys. Rev. Research* **6**, no. 2, 023162 (2024). <https://doi.org/10.1103/PhysRevResearch.6.023162>
- [11] M. I. Dykman, C. M. Maloney, V. N. Smelyanskiy, and M. Silverstein, Fluctuational phase-flip transitions in parametrically driven oscillators, *Phys. Rev. E* **57**, no. 5, 5202–5212 (1998). <https://doi.org/10.1103/PhysRevE.57.5202>
- [12] L. J. Lapidus, D. Enzer, and G. Gabrielse, Stochastic phase switching of a parametrically driven electron in a penning trap, *Phys. Rev. Lett.* **83**, no. 15, 899–902 (1999). <https://doi.org/10.1103/PhysRevLett.83.899>

- [13] M. Marthaler and M. I. Dykman, Switching via quantum activation: A parametrically modulated oscillator, *Phys. Rev. A* **73**, no. 4, 042108 (2006). <https://doi.org/10.1103/PhysRevA.73.042108>
- [14] K. Kim, M. S. Heo, K. H. Lee, K. Jang, H. R. Noh, D. Kim, and W. Jhe, Spontaneous symmetry breaking of population in a nonadiabatically driven atomic trap: An Ising-class phase transition, *Phys. Rev. Lett.* **96**, no. 15, 150601 (2006). <https://doi.org/10.1103/PhysRevLett.96.150601>
- [15] H. B. Chan and C. Stambaugh, Activation barrier scaling and crossover for noise-induced switching in micromechanical parametric oscillators, *Phys. Rev. Lett.* **99**, no. 6, 060601 (2007). <https://doi.org/10.1103/PhysRevLett.99.060601>
- [16] E. Goto, The Parametron, a Digital Computing Element Which Utilizes Parametric Oscillation, in *Proceedings of the IRE* **47**, no. 8, 1304–1316 (1959). <https://www.doi.org/10.1109/JRPROC.1959.287195>
- [17] I. Mahboob and H. Yamaguchi, Bit storage and bit flip operations in an electromechanical oscillator, *Nat. Nanotechnol.* **3**, no. 5, 275–279 (2008). <https://doi.org/10.1038/nano.2008.84>
- [18] Z. Wang, A. Marandi, K. Wen, R. L. Byer, and Y. Yamamoto, Coherent Ising machine based on degenerate optical parametric oscillators, *Phys. Rev. A* **88**, no. 6, 063853 (2013). <https://doi.org/10.1103/PhysRevA.88.063853>
- [19] P. L. McMahon, A. Marandi, Y. Haribara, R. Hamerly, C. Langrock, S. Tamate, T. Inagaki, H. Takesue, S. Utsunomiya, K. Aihara, R. L. Byer, M. M. Fejer, H. Mabuchi, and Y. Yamamoto, A fully programmable 100-spin coherent Ising machine with all-to-all connections, *Science* **354**, no. 6312, 614–617 (2016). <https://doi.org/10.1126/science.aah5178>
- [20] T. L. Heugel, O. Zilberberg, C. Marty, R. Chitra, and A. Eichler, Ising machines with strong bilinear coupling, *Phys. Rev. Res.* **4**, no. 1, 013149 (2022). <https://doi.org/10.1103/PhysRevResearch.4.013149>
- [21] P. Álvarez, D. Pittilini, F. Miserocchi, S. Raamamurthy, G. Margiani, O. Ameye, J. del Pino, O. Zilberberg, and A. Eichler, Biased Ising Model Using Two Coupled Kerr Parametric Oscillators with External Force, *Phys. Rev. Lett.* **132**, no. 20, 207401 (2024). <https://doi.org/10.1103/PhysRevLett.132.207401>
- [22] A. Leuch, L. Papariello, O. Zilberberg, C. L. Degen, R. Chitra, and A. Eichler, Parametric

- symmetry breaking in a nonlinear resonator, *Phys. Rev. Lett.* **117**, no. 21, 214101 (2016). <https://doi.org/10.1103/PhysRevLett.117.214101>
- [23] D. Ryvkine and M. I. Dykman, Resonant symmetry lifting in a parametrically modulated oscillator, *Phys. Rev. E* **74**, no. 6, 061118 (2006). <https://doi.org/10.1103/PhysRevE.74.061118>
- [24] M. Frimner, T. L. Heugel, Ž. Nosan, F. Tebbenjohanns, D. Hälg, A. Akin, C. L. Degen, L. Novotny, R. Chitra, O. Zilberberg, and A. Eichler, Rapid flipping of parametric phase states, *Phys. Rev. Lett.* **123**, no. 25, 254102 (2019). <https://doi.org/10.1103/PhysRevLett.123.254102>
- [25] Ž. Nosan, P. Märki, N. Hauff, C. Knaut, and A. Eichler, Gate-controlled phase switching in a parametron, *Phys. Rev. E* **99**, no. 6, 062205 (2019). <https://doi.org/10.1103/PhysRevE.99.062205>
- [26] L. Papariello, O. Zilberberg, A. Eichler, and R. Chitra, Ultrasensitive hysteretic force sensing with parametric nonlinear oscillators, *Phys. Rev. E* **94**, no. 2, 022201 (2016). <https://doi.org/10.1103/PhysRevE.94.022201>
- [27] M. C. Lemme, S. Wagner, K. Lee, X. Fan, G. J. Verbiest, S. Wittmann, S. Lukas, R. J. Dolleman, F. Niklaus, H. S. J. van der Zant, G. S. Duesberg, and P. G. Steeneken, Nanoelectromechanical sensors based on suspended 2D materials, *Research* **2020**, 1–25, Art. no. 8748602 (2020).
- [28] B. Xu, P. Zhang, J. Zhu, Z. Liu, A. Eichler, X.-Q. Zheng, J. Lee, A. Dash, S. More, S. Wu, Y. Wang, H. Jia, A. Naik, A. Bachtold, R. Yang, P. X.-L. Feng, and Z. Wang, Nanomechanical Resonators: Toward Atomic Scale. *ACS Nano* **16**, no. 10, 15545–15585 (2022). <https://doi.org/10.1021/acsnano.2c01673>
- [29] V. Sazonova, Y. Yaish, H. Üstünel, D. Roundy, T. A. Arias, and P. L. McEuen, A tunable carbon nanotube electromechanical oscillator, *Nature* **431**, no. 7006, 284–287 (2004). <https://doi.org/10.1038/nature02905>
- [30] Q. Unterreithmeier, E. Weig, and J. Kotthaus, Universal transduction scheme for nanomechanical systems based on dielectric forces, *Nature* **458**, no. 7241, 1001–1004 (2009). <https://doi.org/10.1038/nature07932>
- [31] J. P. Mathew, R. N. Patel, A. Borah, R. Vijay, and M. M. Deshmukh, Dynamical strong coupling and parametric amplification of mechanical modes of graphene drums, *Nat. Nanotech.*

- 11**, no. 9, 747–751 (2016). <https://doi.org/10.1038/nnano.2016.94>
- [32] Z.-J. Su, Y. Ying, X.-X. Song, Z.-Z. Zhang, Q.-H. Zhang, G. Cao, H.-O. Li, G.-C. Guo, and G.-P. Guo, Tunable parametric amplification of a graphene nanomechanical resonator in the nonlinear regime, *Nanotechnology* **32**, no. 15, 155203 (2021). <https://doi.org/10.1088/1361-6528/abc9ea>
- [33] J. S. Aldridge and A. N. Cleland, Noise-Enabled Precision Measurements of a Duffing Nanomechanical Resonator, *Phys. Rev. Lett.* **94**, no. 15, 156403 (2005). <https://doi.org/10.1103/PhysRevLett.94.156403>
- [34] I. Kozinsky, H. W. Ch. Postma, I. Bargatin, and M. L. Roukes, Tuning nonlinearity, dynamic range, and frequency of nanomechanical resonators, *Appl. Phys. Lett.* **88**, no. 25, 253101 (2006). <https://doi.org/10.1063/1.2209211>
- [35] C. Chen, S. Rosenblatt, K. I. Bolotin, W. Kalb, P. Kim, I. Kymissis, H. L. Stormer, T. F. Heinz, and J. Hone, Performance of monolayer graphene nanomechanical resonators with electrical readout, *Nat. Nanotech.* **4**, no. 12, 861–867 (2009). <https://doi.org/10.1038/nnano.2009.267>
- [36] Q. P. Unterreithmeier, T. Faust, and J. P. Kotthaus, Nonlinear switching dynamics in a nanomechanical resonator, *Phys. Rev. B* **81**, no. 24, 241405R (2010). <https://doi.org/10.1103/PhysRevB.81.241405>
- [37] A. Eichler, J. Moser, J. Chaste, M. Zdrojek, I. Wilson-Rae, and A. Bachtold, Nonlinear damping in mechanical resonators made from carbon nanotubes and graphene, *Nat. Nanotech.* **6**, no. 6, 339–342 (2011). <https://doi.org/10.1038/nnano.2011.71>
- [38] M. I. Dykman and M. A. Krivoglaz, Spectral distribution of nonlinear oscillators with nonlinear friction due to a medium, *Phys. Status Solidi B* **68**, no. 1, 111–123 (1975). <https://doi.org/10.1002/pssb.2220680109>
- [39] S. Zaitsev, O. Shtempluck, E. Buks, and O. Gottlieb, Nonlinear damping in a micromechanical oscillator, *Nonlinear Dyn.* **67**, no. 1, 859–883 (2012). <https://doi.org/10.1007/s11071-011-0031-5>
- [40] A. M. van der Zande, R. A. Barton, J. S. Alden, C. S. Ruiz-Vargas, W. S. Whitney, P. H. Q. Pham, J. Park, J. M. Parpia, H. G. Craighead, and P. L. McEuen, Large-Scale Arrays of Single-Layer Graphene Resonators, *Nano. Lett.* **10**, no. 12, 4869–4873 (2010). <https://doi.org/10.1021/nl102713c>

- [41] J. S. Bunch, A. M. V. D. Zande, S. S. Verbridge, I. W. Frank, D. M. Tanenbaum, J. M. Parpia, H. G. Craighead, and P. L. McEuen, Electromechanical resonators from graphene sheets, *Science* **315**, no. 5811, 490–493 (2007). <https://doi.org/10.1126/science.1136836>
- [42] R. A. Barton, I. R. Storch, V. P. Adiga, R. Sakakibara, B. R. Cipriany, B. Ilic, S. P. Wang, P. Ong, P. L. McEuen, J. M. Parpia, and H. G. Craighead, Photothermal self-oscillation and laser cooling of graphene optomechanical systems, *Nano Lett.* **12**, no. 9, 4681–4686 (2012). <https://doi.org/10.1021/nl302036x>
- [43] D. Davidovikj, J. J. Slim, S. J. Cartamil-Bueno, H. S. J. van der Zant, P. G. Steeneken, and W. J. Venstra, Visualizing the motion of graphene nanodrums, *Nano Lett.* **16**, no. 4, 2768–2773 (2016). <https://doi.org/10.1021/acs.nanolett.6b00477>
- [44] H. Lu, C. Yang, Y. Tian, J. Lu, F. Xu, C. Zhang, F. Chen, Y. Ying, K. G. Schädler, C. Wang, F. H. L. Koppens, A. Reserbat-Plantey, and J. Moser, Imaging vibrations of electromechanical few layer graphene resonators with a moving vacuum enclosure, *Precis. Eng.* **72**, 769–776 (2021). <https://doi.org/10.1016/j.precisioneng.2021.06.012>
- [45] J. J. Hopfield, Neural networks and physical systems with emergent collective computational abilities, *Proc. Natl. Acad. Sci. USA* **79**, no. 8, 2554–2558 (1982). <https://doi.org/10.1073/pnas.79.8.2554>
- [46] D. Krotov, A new frontier for Hopfield networks, *Nat. Rev. Phys.* **5**, no. 7, 366–367 (2023). <https://doi.org/10.1038/s42254-023-00595-y>
- [47] C. Lucibello and M. Mézard, Exponential capacity of dense associative memories, *Phys. Rev. Lett.* **132**, no. 7, 077301 (2024). <https://doi.org/10.1103/PhysRevLett.132.077301>
- [48] R. J. Glauber, Time-dependent statistics of the Ising model, *J. Math. Phys.* **4**, no. 2, 294–307 (1963). <https://doi.org/10.1063/1.1703954>
- [49] H. Sompolinsky and I. Kanter, Temporal association in asymmetric neural networks, *Phys. Rev. Lett.* **57**, no. 22, 2861–2864 (1986). <https://doi.org/10.1103/PhysRevLett.57.2861>
- [50] M. Aguilera, S. A. Moosavi, and H. Shimazaki, A unifying framework for mean-field theories of asymmetric kinetic Ising systems, *Nat. Commun.* **12**, no. 1, 1197 (2021). <https://doi.org/10.1038/s41467-021-20890-5>
- [51] M. Fruchart, R. Hanai, P. B. Littlewood, and V. Vitelli, Nonreciprocal phase transitions, *Nature* **592**, no. 7854, 363–369 (2021). <https://doi.org/10.1038/s41586-021-03375-9>